



HAL
open science

Catalytic activation of a non-noble intermetallic surface through nanostructuring under hydrogenation conditions revealed by atomistic thermodynamics

Émilie Gaudry, Corentin Chatelier, David Loffreda, Dmytro Kandaskalov, Alessandro Coati, Laurent Piccolo

► **To cite this version:**

Émilie Gaudry, Corentin Chatelier, David Loffreda, Dmytro Kandaskalov, Alessandro Coati, et al.. Catalytic activation of a non-noble intermetallic surface through nanostructuring under hydrogenation conditions revealed by atomistic thermodynamics. *Journal of Materials Chemistry A*, 2020, 8 (15), pp.7422-7431. 10.1039/D0TA01146K . hal-02548908

HAL Id: hal-02548908

<https://hal.science/hal-02548908v1>

Submitted on 11 Sep 2020

HAL is a multi-disciplinary open access archive for the deposit and dissemination of scientific research documents, whether they are published or not. The documents may come from teaching and research institutions in France or abroad, or from public or private research centers.

L'archive ouverte pluridisciplinaire **HAL**, est destinée au dépôt et à la diffusion de documents scientifiques de niveau recherche, publiés ou non, émanant des établissements d'enseignement et de recherche français ou étrangers, des laboratoires publics ou privés.

Cite this: DOI: 00.0000/xxxxxxxxxx

Catalytic activation of a non-noble intermetallic surface through nanostructuring under hydrogenation conditions revealed by atomistic thermodynamics †

É. Gaudry^{*a}, C. Chatelier^{a,b}, D. Loffreda^c, D. Kandaskalov^d, A. Coati^b, L. Piccolo^e

Received Date

Accepted Date

DOI: 00.0000/xxxxxxxxxx

The unique electronic and crystallographic structure of intermetallics is known to result in excellent catalytic performances for selected chemical reactions. Moreover, owing to the specific bonding network of these compounds, a high structural stability of their surfaces is generally assumed, even under reaction conditions. Transition metal (TM = Fe, Co) aluminides of the $\text{Al}_{13}\text{TM}_4$ stoichiometry have previously demonstrated high activities and selectivities in partial hydrogenation of alkynes and alkadienes. Focusing on the $\text{Al}_{13}\text{Co}_4(100)$ surface as a model catalyst for butadiene hydrogenation, the hydrogen-rich reaction conditions are predicted – based on DFT calculations and atomistic thermodynamics – to modify the relatively flat surface structure identified under ultra-high vacuum, in the form of highly cohesive clusters emerging from the bulk lattice. Unlike the flat one, this termination presents favorable adsorption properties, able to make it catalytically active and fully selective to butenes. In addition, its contrasted catalytic behavior as compared to that of the reference $\text{Al}_{13}\text{Fe}_4(010)$ surface – which is more active but less selective – is rationalized in terms of butadiene, butene and hydrogen co-adsorption properties. This work demonstrates that a realistic description of the surface structures under reaction conditions is mandatory to the design of new-generation catalysts based on the complex topology of intermetallic surfaces.

1 Introduction

Heterogeneous catalysis on intermetallic compounds represents a quickly growing field, which contributed to innovative breakthroughs in recent years. Several examples show the possible replacement of noble metal-based materials with noble metal-free intermetallics for selective hydrogenation reactions^{1–7}. The catalytic performances of these compounds are ascribed to their stability, as well as their defined stoichiometries and ordered crystal structures. This leads to unique coordination geometries^{8–10}, and to isolated active sites. The latter especially holds in the case of complex intermetallic compounds, a class of ordered alloys comprising quasicrystals, their approximants and other ordered compounds with large unit cells^{11,12}.

The stabilization of intermetallics bulk crystal structures and stoichiometries, which constitutes a key advantage over transition metal alloys, is generally explained by electronic factors of various types (Mott-Jones mechanism¹³, Zintl concept¹⁴, etc). This is assumed to lead to stable surfaces, even under reaction conditions^{2,15,16}. However, investigations to probe a possible adsorbate-induced restructuring in the case of complex intermetallics surfaces under hydrogenation conditions, and its influence on the catalytic performances, have never been reported to our knowledge. With respect to simple metal/alloy catalysts that can already face surface reconstruction, segregation, roughening, or more macroscopic restructuring under reaction conditions¹⁷, additional phenomena are expected when dealing with complex intermetallic catalysts. In particular, their structural building blocks, i. e. highly symmetric clusters of a few tens of atoms¹⁸ may influence their surface structure and related catalytic properties.

$\text{Al}_{13}\text{TM}_4$ (TM = Fe, Co) complex intermetallic compounds have recently shown unexpected performances in the partial hydrogenation of alkynes^{2,19} and alkadienes^{4,20,21}. The bulk and surface structures of these compounds, considered as low scale prototypes of Al-based decagonal quasicrystals, have been extensively studied since several years^{22–32}. A possible reaction path

^aUniversité de Lorraine, CNRS, IJL, F-54000 Nancy, France; E-mail: Emilie.Gaudry@univ-lorraine.fr

^bSynchrotron SOLEIL, L'Orme des Merisiers, Saint-Aubin, France

^cUniv. Lyon - Ens de Lyon, CNRS Univ. Lyon 1, F-69342 Lyon, France

^dAix Marseille Univ, Univ Toulon, CNRS, IM2NP, Marseille, France

^eUniv. Lyon, Université Claude Bernard Lyon 1, CNRS, IRCELYON, F-69626 Villeurbanne, France

† Electronic Supplementary Information (ESI) available: Computation details, Structural models and energies for adsorption and co-adsorption on $\text{Al}_{13}\text{TM}_4$ pseudo 10-fold surfaces. See DOI: 00.0000/00000000.

was identified by first principles calculations on the $\text{Al}_{13}\text{Co}_4(100)$ surface, with energy barriers similar to the ones calculated for conventional Pd and Pd-Ag catalysts³³. However, the starting point of this investigation was a surface model derived from a theoretical cleavage, which appears to be inconsistent with the experimental observations of the surface prepared by sputtering-annealing under UHV^{23–25}, and for which rather large barriers have been calculated³⁴. Thus the question of the surface structure under catalytic hydrogenation conditions remained open.

On the basis of DFT calculations, reaction conditions are here shown to promote from the relatively flat $\text{Al}_{13}\text{Co}_4(100)$ surface known under UHV, the emergence of bulk-like clusters at the surface. This surface termination is similar to that determined for $\text{Al}_{13}\text{Fe}_4(010)$ under UHV.

Not only the surface atomic structure but also electronic effects associated with the nature of the transition metal are expected to influence the catalytic performances. A recent experimental investigation of the catalytic performances of quasi isostructural $\text{Al}_{13}\text{Co}_4(100)$ and $\text{Al}_{13}\text{Fe}_4(010)$ surfaces for butadiene partial hydrogenation has revealed that the initial butene-formation activity of $\text{Al}_{13}\text{Fe}_4$ is 5-10 times higher than that of $\text{Al}_{13}\text{Co}_4$, while the selectivity to butene is maximum on the latter²¹. In the second step of this work, we rationalize the differences between these two systems, by determining their respective hydrogen adsorption and hydrogen-hydrocarbon co-adsorption properties under reaction conditions.

2 Models and Methods

2.1 $\text{Al}_{13}\text{TM}_4$ (TM=Co, Fe) Bulk and Surface Structures

$\text{Al}_{13}\text{Fe}_4$ crystallizes in the $C2/m$ space group (No. 12, Pearson symbol $mC102$, fig. 1)²⁷. So far, six phases from the $\text{Al}_{13}\text{Co}_4$ family were reported with slightly different structures³⁵. The crystal used in this study (*o*- $\text{Al}_{13}\text{Co}_4$) is orthorhombic and crystallizes in the $Pmn2_1$ space group (No. 31, Pearson symbol $oP102$). It is known to be unstable at low temperatures, but stabilized at higher temperatures by the entropy of Al vacancy hopping and low frequency vibrational modes³⁶. In the following, ideal structures with full atomic occupations are considered.

The bulk structures of $\text{Al}_{13}\text{TM}_4$ compounds, considered as approximants to decagonal quasicrystals, are traditionally described as periodic piles of atomic planes perpendicularly to the pseudo 10-fold direction ($[100]$ and $[010]$ for $\text{Al}_{13}\text{Co}_4$ and $\text{Al}_{13}\text{Fe}_4$, respectively), with pseudo-quasiperiodic in-plane atomic order. Like most intermetallic compounds¹⁸, they are also represented as a stacking of clusters, defined by geometric or electronic arguments^{37–40}. This dual description leads to two typical models for the $\text{Al}_{13}\text{Co}_4(100)$ and $\text{Al}_{13}\text{Fe}_4(010)$ pseudo 10-fold surfaces, presented in Fig. 1. Their relative stabilities depend on the aluminum chemical potential²², i.e. on the exact composition of the single crystalline ingot used for the experiments (amount of vacancies, anti-sites, etc)^{41,42}: a rather flat termination, truncating the cluster substructure, without protruding Co atoms (P^{flat} model) in the Al-rich limit, or a nanostructured termination (P^{corr} model), build from the preservation of the cluster building blocks at the surface, in relation to strong covalent interactions present

in these compounds²², in the TM-rich limit. Other models may be meaningful as well, as suggested by Refs.^{23–26}. We focus here on the two limit cases P^{flat} and P^{corr} , which are relevant for both systems. Besides being experimentally observed under UHV – P^{flat} for $\text{Al}_{13}\text{Co}_4(100)$ and P^{corr} for $\text{Al}_{13}\text{Fe}_4(010)$ – these models have been the bases of previous theoretical investigations of the $\text{Al}_{13}\text{Co}_4(100)$ catalytic performances (P^{flat} ³⁴ and P^{corr} ³³).

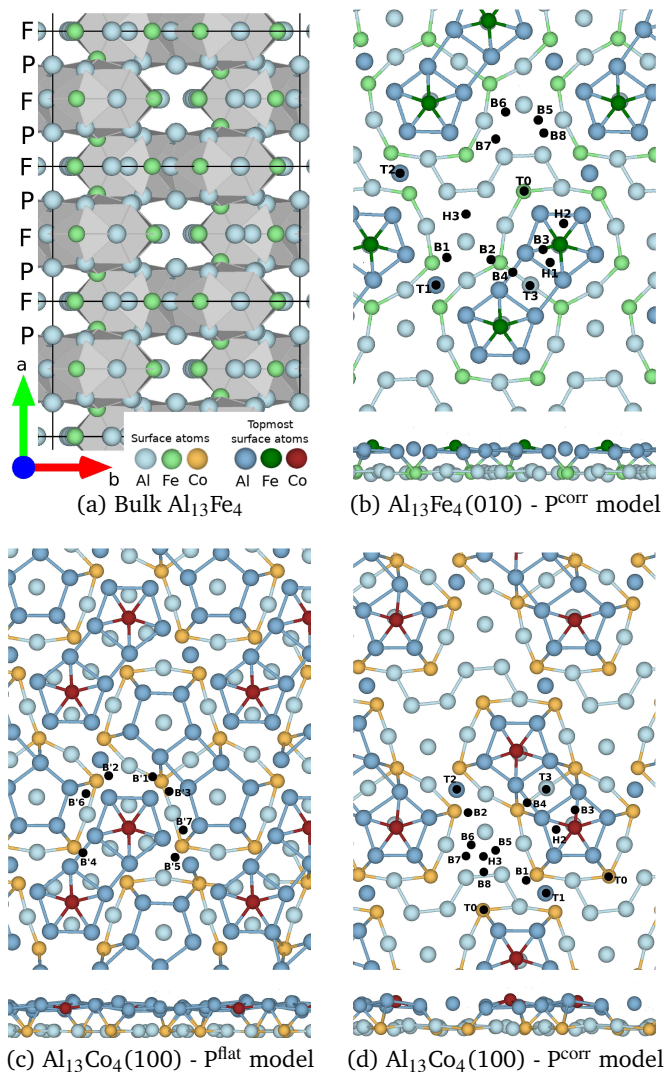


Fig. 1 $\text{Al}_{13}\text{Fe}_4$ bulk structure (a, Henley-type clusters in gray) and surface models (b-d, top and side views) for $\text{Al}_{13}\text{Fe}_4(010)$ and $\text{Al}_{13}\text{Co}_4(100)$. Color code: topmost surface Al, Fe and Co atoms in blue, dark green and dark red, respectively; Al, Fe and Co atoms in light blue, green and orange, respectively.

2.2 Computational details

All calculations are based on DFT and use the Vienna *ab initio* simulation package (VASP). Self-consistent Kohn Sham equations were solved by means of the projected-augmented wave (PAW) method⁴³. Spin polarization was not taken into account, as it is not requested for such Al-rich compounds^{34,36}. The electron exchange and correlation energies were described by the gen-

eralized gradient approximation approach, using the standard semilocal functional (PBE)⁴⁴, known to underestimate several parameters like the surface energy. The magnitude of underestimation has been shown to correlate with the extent to which the functional neglects van der Waals attraction at intermediate and long ranges⁴⁵. Then, the DFT-D3 method⁴⁶ was used to include such effects. The plane-waves energy cut-off was set to 500 eV. Monkhorst-Pack meshes were used for the k -points sampling⁴⁷ ($9 \times 7 \times 5$ and $1 \times 7 \times 5$ k -meshes for $\text{Al}_{13}\text{TM}_4$ bulk systems and surfaces, respectively). For the bulk materials, this leads to structural parameters and cohesive energies in reasonable agreement with the experimental values (Tab. S1, Tab. 1) for both PBE and DFT-D3 functionals.

2.3 Thermodynamic model

Surfaces were modeled with 7-layer-thick symmetric slabs, separated by a void thickness ($\sim 20 \text{ \AA}$). Since the slab stoichiometries differ from those of their bulk, the surface energies are not given by the simple energy difference between slabs and corresponding bulks, as in the case of elemental metals, but involve the chemical potentials (μ_{Al} , μ_{TM}) of the chemical species in the slab (section S1.3)^{48,49}:

$$\gamma_{\text{clean}}(\mu_{\text{Al}}) = \frac{1}{2A} \left[E^{\text{slab}}(N_{\text{Al}}, N_{\text{TM}}) - \mu_{\text{Al}} N_{\text{Al}} - \mu_{\text{TM}} N_{\text{TM}} \right] \quad (1)$$

where A is the area of the surface cell and $E^{\text{slab}}(N_{\text{Al}}, N_{\text{TM}})$ is the total energy of the slab, built with N_{Al} Al and N_{TM} TM species. The chemical potentials of the species are related through the cohesive energy (E_{coh}) of the compounds ($17E_{\text{coh}} = 13\mu_{\text{Al}} + 4\mu_{\text{TM}}$). They are constrained in a range, i.e. $\frac{17}{13}\Delta H_f \leq \mu_{\text{Al}} - \mu_{\text{Al}}^{\text{bulk}} \leq 0$ for Al, where ΔH_f is the formation enthalpy of the complex phase.

Possible modifications of the surface structure under operating conditions (pressure P and temperature T) have been investigated by calculating surface energies modified by adsorption⁵⁰⁻⁵², i. e. $\gamma_{\text{cover}}(T, P, \mu_{\text{Al}}) = \gamma_{\text{clean}}(\mu_{\text{Al}}) + \gamma_{\text{ads}}(P, T)$, where

$$\gamma_{\text{ads}}(P, T) = \frac{1}{A} \left[E^{\text{ads}}(N_{\text{Al}}, N_{\text{TM}}, \sum_X n_X) - E^{\text{slab}}(N_{\text{Al}}, N_{\text{TM}}) - \sum_X n_X \left(E_X - k_B T \ln Z_X + k_B T \ln \frac{P_X}{k_B T} \right) \right] \quad (2)$$

In the previous equation, $E^{\text{ads}}(N_{\text{Al}}, N_{\text{TM}}, \sum_X n_X)$ is the total energy of the slab covered with the species, E_X is the gas phase energies of X , where $X \in \{\text{H}_2, \text{C}_4\text{H}_6, \text{C}_4\text{H}_8\}$, while $2n_{\text{H}_2}$ and $n_{\text{C}_4\text{H}_x}$ are the number of atomic hydrogen atoms and C_4H_x molecules adsorbed in one surface cell, respectively ($x \in \{6, 8\}$, $n_{\text{C}_4\text{H}_x} \in \{0, 1\}$). We only considered the rotational (z_{rot}^X) and modified translational (z_{trans}^X) contributions to the partition function: $Z = z_{\text{trans}}^X z_{\text{rot}}^X$ (Tab. S2). Here, we consider that all translation degrees of freedom for adsorbates are lost when adsorbed, and we do not consider configurational entropy. These contributions are assumed to be small⁵³.

		a (Å)	b (Å)	c (Å)	β (°)	ΔH_f (eV)
$\text{Al}_{13}\text{Co}_4$	PBE	8.20	12.40	14.42	-	-0.385
	D3	8.09	12.25	14.28	-	-0.413
	exp.	8.158	12.342	14.452	-	-0.55 ^{27,54}
$\text{Al}_{13}\text{Fe}_4$	PBE	15.43	8.02	12.43	107.69	-0.329
	D3	15.27	7.92	12.29	107.69	-0.346
	exp.	15.492	8.078	12.471	107.69	-0.30 ^{28,55}

Table 1 Cell parameters and formation enthalpies for bulk $\text{Al}_{13}\text{TM}_4$.

3 Results and Discussion

3.1 Adsorption properties

To predict adsorption thermodynamics at reaction conditions, the first step consists in the determination of the energetically favorable adsorption structures and sites for H, C_4H_6 and C_4H_8 .

3.1.1 Atomic hydrogen

The atomic hydrogen adsorption properties of $\text{Al}_{13}\text{Co}_4(100)$ (P^{flat} model) have been detailed in a previous work within the PBE approximation⁵⁶. The most stable sites are bridge sites (Tab. S3). Overall, the consideration of van der Waals effects leads to a slight stabilization of the adsorbates, by less than 10 meV/at. In all cases, the favorable adsorption sites are stabilized by the electronic donor character of cobalt atoms positioned in the sub-surface layer ($\text{Co}^{\text{S-1}}$)⁵⁶. The potential energy surface of an hydrogen atom is very flat, giving rise to very easy atomic hydrogen diffusion, with barriers smaller than 0.3 eV (PBE functional)³⁴. The dissociative adsorption of H_2 has been shown to occur with a rather low barrier as well (0.59 eV³⁴, PBE functional), even if this surface shows an Al-rich termination.

Only two TM atoms per surface cell protrude at the surface on the incomplete P layer (P^{corr} model), each surrounded by a pentagonal arrangement of Al atoms. The vicinity of these protruding TM atoms provides favorable adsorption sites for atomic hydrogen (sites B3, H1 and H2, see Tab. 2), which result from H_2 dissociative adsorption on top of a TM atom. The barriers for such dissociations are calculated to be low (0.18 eV³³ for $\text{Al}_{13}\text{Co}_4(100)$ and 0.06 eV for $\text{Al}_{13}\text{Fe}_4(010)$, within the PBE approach). Another favorable site is the one on top of the under coordinated Al “glue atom” (sites T1 and T2). However, these surface Al atoms may desorb at high temperatures. In that case, hydrogen atoms may adsorb on the underlying TM atom, with a similar adsorption energy for $\text{Al}_{13}\text{Fe}_4(010)$ (-0.50 eV within the PBE approach) and a slightly reduced one for $\text{Al}_{13}\text{Co}_4(100)$ (-0.29 eV³³, within the PBE approach). Similar trends are found with the DFT-D3 functional. One interesting result is related to the adsorption process occurring on the Al-Al bridge sites (B4), calculated to be exothermic on $\text{Al}_{13}\text{Co}_4(100)$ and endothermic on $\text{Al}_{13}\text{Fe}_4(010)$. For the semi-hydrogenation of acetylene on $\text{Al}_{13}\text{Co}_4(100)$, this bridge adsorption site was found to be crucial to ensure the diffusion from the source of atomic hydrogen to the catalytically active site³³. This raises the question of the transferability of the reaction path calculated on $\text{Al}_{13}\text{Co}_4(100)$ to $\text{Al}_{13}\text{Fe}_4(010)$, at least for the semi-hydrogenation of acetylene.

Only a few sites are found to be favorable for hydrogen adsorp-

Site			Al ₁₃ Fe ₄ (010)		Al ₁₃ Co ₄ (100)	
			PBE	DFT-D3	PBE	DFT-D3
Top sites						
T0	TM	S-1	-0.52	-0.61	-0.18	-0.25
T1	Al	S	-0.52	-0.55	-0.43	-0.45
T2	Al	S	-0.54	-0.57	-0.49	-0.51
T3	Al	S-1	0.36	0.28	0.36	0.28
Bridge sites						
B1	Al-TM	S-1	-0.09	-0.19	0.18	0.11
B2	Al-TM	S-1	-0.19	-0.28	0.10	0.04
B3	Al-TM	S	-0.39	-0.44	-0.18	-0.24
B4	Al-Al	S	0.08	0.03	-0.19	-0.25
B5	Al-Al	S-1	0.35	0.30	-0.06	-0.17
B6	Al-Al	S-1	0.55	0.50	0.07	0.01
B7	Al-Al	S-1	0.53	0.49	0.11	0.01
B8	Al-Al	S-1	0.11	0.05	-0.14	-0.21
Hollow sites						
H1	2 Al, 1 TM	S	-0.41	-0.47		
H2	2 Al, 1 TM	S	-0.47	-0.53	-0.13	-0.18
H3	3 Al	S-1	0.25	0.18	0.52	0.47

Table 2 Atomic hydrogen adsorption energies (eV) calculated on the nanostructured surface model (P^{corr}).

tion on the exposed part of the Al₁₃TM₄ F-type layer (P^{corr} model). While the adsorption energies are calculated to be as high as on the topmost P-type layer (site B3), the types of favorable adsorption sites are quite distinct on the two Al₁₃TM₄ surfaces: they are mostly Al-Fe bridge sites (B2, B3) on Al₁₃Fe₄(010), hydrogen atoms being located very close to the Fe atom ($d_{\text{H-Fe}} = 1.55 - 1.57$ Å), while a few Al-Al bridge sites (B8) are found to be favorable on Al₁₃Co₄(100). The positive adsorption energy calculated with atomic hydrogen positioned in the subsurface (site T3) is consistent with the suppression of hydride formation already observed with these materials². Again, the consideration of van der Waals interactions does not modify much the picture drawn using the PBE functional.

The previous results are then used to build hydrogenated surface models with hydrogen coverages ranging from one to twelve hydrogen atoms per cell (5.6×10^{-3} Å² to 6.7×10^{-2} Å⁻², Figs. S1-S3). The complex energy landscape displayed by the pseudo 10-fold surface leads to a non-monotonous character of the atomic hydrogen differential adsorption energies.

3.1.2 1,3-Butadiene and But-1-ene

Regardless the surface model, the trans configuration of butadiene is preferred (Tab. 3), the molecule-surface interaction occurring through π -bonds, di- σ -bonds or a combination of both types. On the P^{corr} model, all considered adsorption sites involve protruding surface TM atoms and neighboring Al atoms. No adsorption sites were found in between the surface clusters, on the exposed part of the F-type layer. Only surface Al atoms are involved in the case of the P^{flat} model.

The adsorption energies of butadiene calculated on Al₁₃Co₄(100) range from -0.76 eV to -1.06 eV within the PBE approach, and from -1.31 eV to -1.59 eV using the DFT-D3 functional, hence demonstrating the stabilizing effect of dispersion between the adsorbate and the substrate. The energetic ordering between the optimal adsorption structures is globally

kept from PBE to DFT-D3 functionals. The unsaturated molecule is more strongly adsorbed on Al₁₃Fe₄(010). The surface energy landscape is also found to be flatter, the range of butadiene adsorption energy differences being below 100 meV, using both the PBE and DFT-D3 functionals. The stronger adsorption of butadiene on Al₁₃Fe₄(010) than on Al₁₃Co₄(100), classically attributed to a decreased filling of the adsorbate-metal antibonding states, is indeed in agreement with Bader charge calculations (section S5) and the lower-energy d-band center in the former case: -1.41 eV for bulk Al₁₃Fe₄, -1.97 eV for bulk Al₁₃Co₄²¹.

A few configurations are presented for butene on Al₁₃Co₄(100) and Al₁₃Fe₄(010) (Tab. 4). On the P^{corr} model, the π configuration is the most favorable, whatever is the relative orientation of the molecule with respect to the surface. On the P^{flat} model, the most stable configuration is found to be a di- σ configuration, the adsorption energy being rather similar to the one found for the π configurations on the P^{corr} models^{57,58}. In all cases, butene adsorption is found to be weaker than butadiene adsorption.

The adsorption of alkene molecules on TM-A binaries where A is a sp metal, generally only involves the TM surface atoms. It is the case for ethene on the pseudo 5-fold surface of GaPd⁵⁹ and AlPd⁶⁰, as well as for ethene, butadiene and propene on Pt₅Sn/Pt(111)⁶¹⁻⁶⁴. The role played by surface Al atoms on the molecule-surface bonding has already been explored using acetylene on the Al₅Co₂(2 $\bar{1}$ 0) and Al₁₃Co₄(100) surfaces^{33,56,65}. On the Al₁₃TM₄ pseudo 10-fold surfaces, two factors may explain the role played by surface Al atoms in the bonding: the low coordination of Al atoms in the vicinity of protruding TM atoms, in the case of the P^{corr} model, as well as the covalent-like character of Al-TM bonds.

3.2 Nanostructuring of Al₁₃Co₄(100) under reaction conditions

The butadiene hydrogenation reaction is known to follow a Horiuti-Polanyi-type mechanism⁶⁶, which requires the presence of coadsorbed {butadiene+hydrogen} species. These adsorbates may induce modifications of the surface structure. This is questioned here in the case of Al₁₃Co₄(100), using the previous surface models and adsorption energies as inputs for the thermodynamic model introduced before.

3.2.1 Hydrogenated Al₁₃Co₄(100) surfaces

The stability phase diagrams of hydrogenated surfaces are drawn for three different pressures, simulating industrial catalysis (2 bar)⁶⁷ and UHV conditions ($5 \cdot 10^{-10}$ mbar), as well as the reaction conditions of Ref.²¹ (Fig. 2).

Under UHV, and for $T = 300$ K, the two surface models are calculated to be “clean”, i.e. without any hydrogen atom adsorbed. Then, the hydrogen coverage increases progressively as the temperature decreases and the pressure increases. On the P^{flat} model, the surface remains bare when $P = 5$ mbar and $T = 300$ K, within the PBE approach, while a slightly larger hydrogen coverage (2 H per surface cell) is found, with the same conditions, within the DFT-D3 approach. Overall, on the P^{corr} model, the hydrogen coverage is found to be higher. For $T = 300$ K and $P = 5$ mbar, it reaches 2 and 6 atoms per surface cell, using the PBE and DFT-

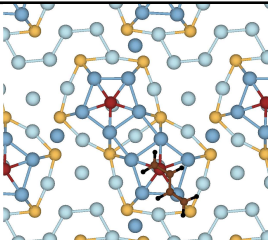
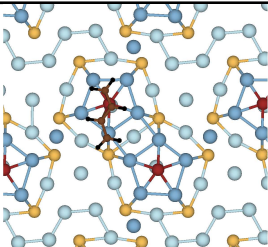
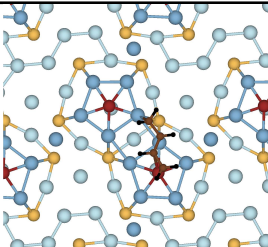
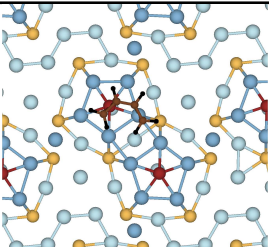
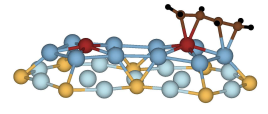
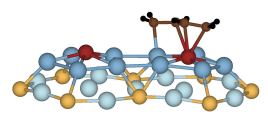
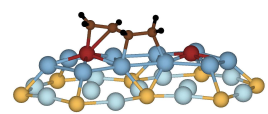
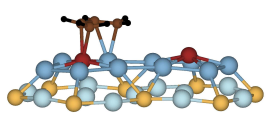
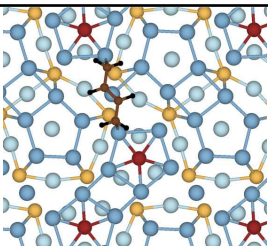
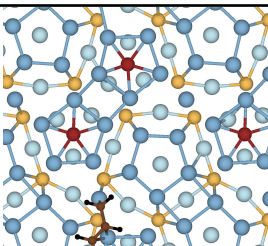
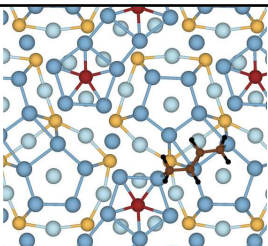
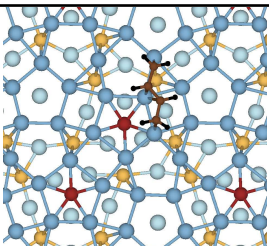
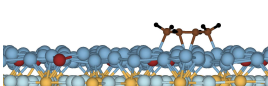
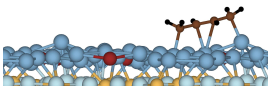
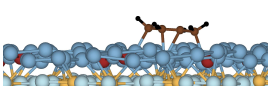
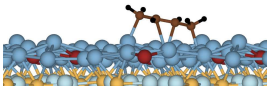
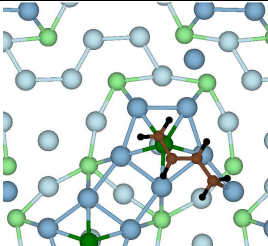
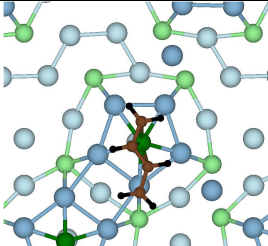
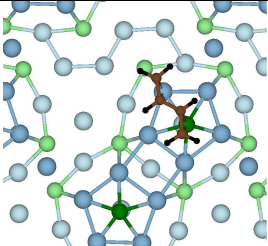
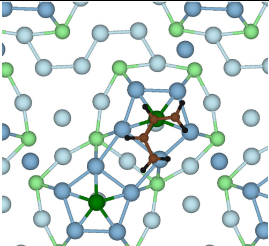
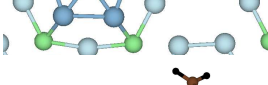

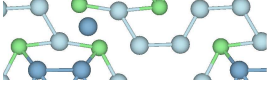

Al ₁₃ Co ₄ (100) p ^{corr} model				
				
PBE	-1.06	-0.99	-0.74	-0.76
DFT-D3	-1.59	-1.53	-1.26	-1.31
Al ₁₃ Co ₄ (100) p ^{flat} model				
				
PBE	-1.24	-1.11	-1.08	-1.02
DFT-D3	-1.90	-1.75	-1.75	-1.67
Al ₁₃ Fe ₄ (010) p ^{corr} model				
				
PBE	-1.34	-1.36	-1.30	-1.28
DFT-D3	-1.94	-1.90	-1.83	-1.85

Table 3 Butadiene adsorption geometries (top and perspective views) and energies (eV).

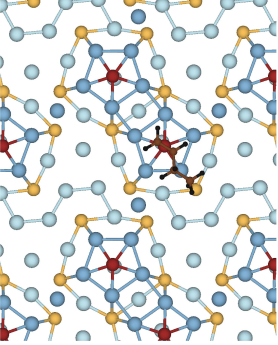
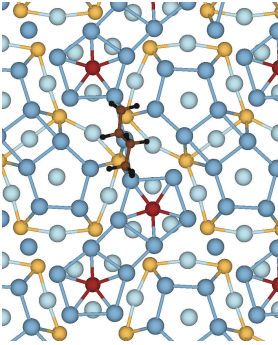
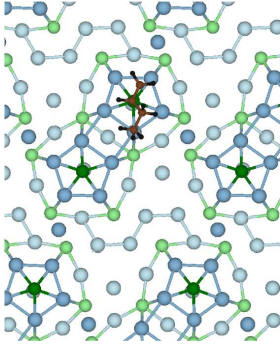
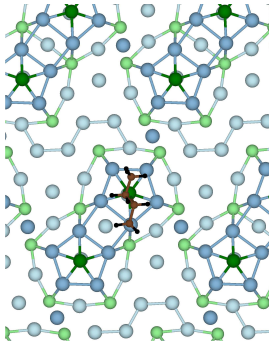
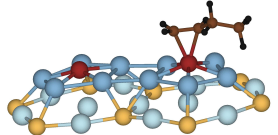
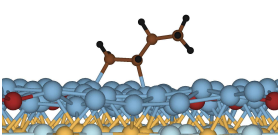
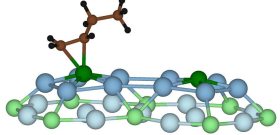
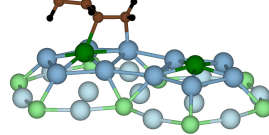
	Al ₁₃ Co ₄ (100) p ^{corr}	Al ₁₃ Co ₄ (100) p ^{flat}	Al ₁₃ Fe ₄ (010) p ^{corr}	Al ₁₃ Fe ₄ (010) p ^{corr}
				
				
PBE	-0.62	-0.65	-0.91	0.08
DFT-D3	-1.13	-1.26	-1.38	-0.31

Table 4 But-1-ene adsorption energies (eV) on Al₁₃Co₄(100) and Al₁₃Fe₄(010)

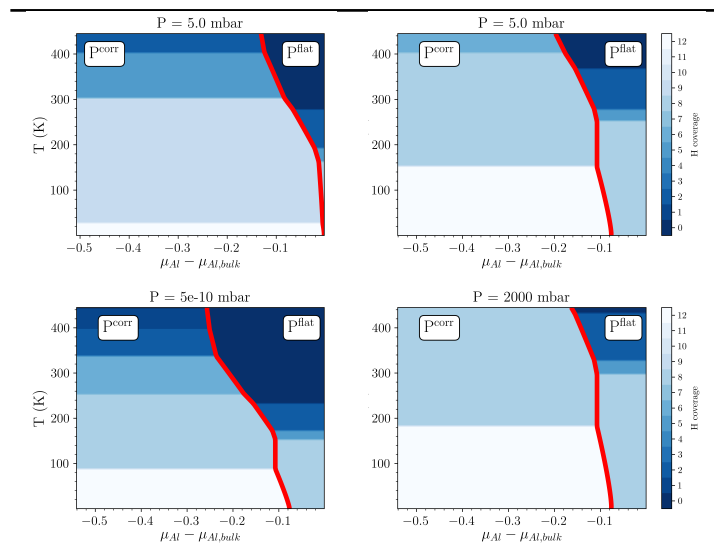


Fig. 2 Surface phase diagrams and optimal hydrogen coverages (number of hydrogen atoms in the surface cell) for the hydrogenated Al₁₃Co₄(100) surface within the PBE (upper left panel) and DFT-D3 (other panels). The red line corresponds to $\gamma_{cover}^{p^{corr}}(P, T, \mu_{Al}) - \gamma_{cover}^{p^{flat}}(P, T, \mu_{Al}) = 0$.

D3 functionals, respectively, and it increases up to 8-9 atoms per surface cell for $P = 2$ bar.

In all cases, the corrugated surface model (P^{corr}) is the most stable one in the Co-rich limit while the flat surface model (P^{flat}) is the most stable one in the Al-rich limit. This is similar to what was found using standard DFT ($T = 0, P = 0$), and in agreement with experimental observations^{23–25}. However, the reaction conditions quite significantly affect the region $\mathcal{A}_{p^{flat}}$ where the P^{flat} model is more stable than the P^{corr} model ($\gamma_{cover}^{p^{corr}}(P, T, \mu_{Al}) \geq \gamma_{cover}^{p^{flat}}(P, T, \mu_{Al})$ and $\mu_{Al} \leq \mu_{Al}^{bulk}$). Indeed, since atomic hydrogen adsorption is calculated to be more favorable on the P^{corr} model, and since exothermic adsorption on solid surfaces contributes to reduce their surface energy, a narrowing of $\mathcal{A}_{p^{flat}}$ occurs as the pressure increases and the temperature decreases. Within the PBE approach, $\mathcal{A}_{p^{flat}}$ almost vanishes when $P = 2$ bar. Using the DFT-D3 approximation, $\mathcal{A}_{p^{flat}}$ extends to a wider range of chemical potentials.

3.2.2 Coadsorption {H+C₄H₆} on Al₁₃Co₄(100)

Atomic hydrogen and C₄H₆ need to be simultaneously adsorbed on the surface for the hydrogenation reaction to occur according to the Langmuir–Hinshelwood mechanism⁶⁶. We consider coadsorption with one butadiene molecule adsorbed per surface unit cell and a variable surface coverage of adsorbed hydrogen atoms (Figs S4-S5). The most stable isolated adsorption structure is considered for butadiene (configurations are shown in the SI) and the gas phase contains H₂ and C₄H_x ($x \in \{6, 8\}$) in the ratio 10:1 as in Ref.²¹ (Fig. 3). Overall, the trends already observed for the hydrogenated surfaces are reproduced here. The optimal hydrogen coverage is however found lower, due to the steric hindrance caused by the presence of the adsorbed butadiene molecule. The consideration of van der Waals interactions does not affect the hydrogen coverage, but leads to a narrowing of the $\mathcal{A}_{p^{flat}}$ stability

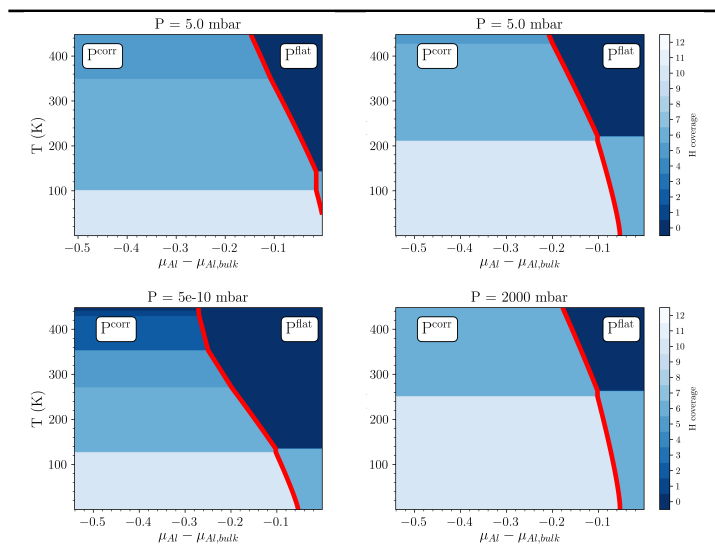


Fig. 3 Surface phase diagrams and optimal hydrogen coverages (number of hydrogen atoms in the surface cell) for $\text{Al}_{13}\text{Co}_4(100)$ covered with butadiene and hydrogen within the PBE (upper left panel) and DFT-D3 (other panels). The red line corresponds to $\gamma_{\text{cover}}^{\text{P}^{\text{corr}}}(P, T, \mu_{\text{Al}}) - \gamma_{\text{cover}}^{\text{P}^{\text{flat}}}(P, T, \mu_{\text{Al}}) = 0$.

domain, similarly to the case of pure hydrogenated surfaces.

3.3 Catalytic activation of $\text{Al}_{13}\text{Co}_4(100)$

Our calculations suggest a nanostructuring of the surface under hydrogenation conditions, for intermediate values of the chemical potentials. For instance, the most stable hydrogenated surface model is the nanostructured P^{corr} model (9 H at./surf. cell) when $P > 5$ mbar, $\Delta\mu_{\text{Al}} = -0.1$ eV and $T = 300$ K, while it is the clean (non-hydrogenated) P^{flat} model under ultra-high vacuum conditions. Co-adsorption does not change the previous picture. The hydrogen coverage value, as well as the stability domains of the P^{corr} and P^{flat} surface models in realistic temperature and pressure conditions are influenced by the choice of the functional. However, in all cases, the clusters already present in the bulk substructure are predicted to emerge at the surface under hydrogenation conditions, for intermediate values of the chemical potentials.

Supplementary arguments are provided by the comparison of our theoretical results with experimental observations. At $T = 300$ K, even for $P = 2$ bar, no hydrogen atom is coadsorbed with butadiene on the P^{flat} surface, which prevents any reaction. This conclusion is valid within both the PBE and DFT-D3 calculations. The P^{corr} model is expected to be more reactive, with 6 hydrogen atoms coadsorbed when $P > 5$ mbar. Since the P^{flat} surface model was identified under UHV conditions^{23–25}, and $\text{Al}_{13}\text{Co}_4(100)$ was experimentally proved to be active and selective²¹, our results predict an activation of $\text{Al}_{13}\text{Co}_4(100)$ under reactive conditions.

3.4 Hydrogenation reaction: $\text{Al}_{13}\text{Co}_4(100)$ vs. $\text{Al}_{13}\text{Fe}_4(010)$

The next step is the comparison of the adsorption energies of butadiene and butene, in operating conditions. We focus here on

the P^{corr} model only. Indeed, the P^{flat} model has been found to be not reactive in the case of $\text{Al}_{13}\text{Co}_4(100)$, no hydrogen atom being coadsorbed under hydrogenation conditions. In addition, it has never been observed experimentally for $\text{Al}_{13}\text{Fe}_4(010)$.

Within the PBE approximation, the optimal hydrogen coverage is found identical for $\text{Al}_{13}\text{Co}_4(100)$ and $\text{Al}_{13}\text{Fe}_4(010)$ (6 at./surf. cell, Figs. 3, S6-S8). The corresponding butadiene and butene free enthalpies are shown in Fig. 4. A weak adsorption is calculated for butadiene on $\text{Al}_{13}\text{Co}_4(100)$ at $(P, T) = (5 \text{ mbar}, 383 \text{ K})$, as well as a spontaneous desorption of butene, without possible further hydrogenation. In contrast, a rather strong adsorption is calculated for both molecules on $\text{Al}_{13}\text{Fe}_4(010)$: once the butadiene molecule has been hydrogenated, the butene product remains adsorbed on the surface and may be further hydrogenated. Our calculations at the thermodynamic level are consistent with experimental observations in the same (P, T) conditions, showing a selective partial hydrogenation of butadiene²¹: a close to 100% selectivity to butenes was found for $\text{Al}_{13}\text{Co}_4(100)$, while a lower value (89% when averaged over the whole semi-hydrogenation period under batch conditions²⁰) was measured with $\text{Al}_{13}\text{Fe}_4(010)$.

The previous picture is modified within the DFT-D3 approximation. Here, the optimal hydrogen coverage is calculated to be 6 and 8 hydrogen atoms per surface cell, on $\text{Al}_{13}\text{Co}_4(100)$ and $\text{Al}_{13}\text{Fe}_4(010)$, respectively (Figs. 3, S5 and S7). The corresponding butadiene and butene free enthalpies are shown in Fig. 5. The comparison with Fig. 4 reveals a shift of the adsorption by ca. 75 K, when considering identical hydrogen coverages. This does not impact our conclusions for $\text{Al}_{13}\text{Fe}_4(010)$, the two molecule still being strongly adsorbed. Butene may also not desorb from $\text{Al}_{13}\text{Co}_4(100)$, allowing further hydrogenation to butane. This behavior, obtained with chemisorbed butene resulting from the hydrogenation of the C=C fragment not bounded to the protruding surface Co atoms, is not consistent with the experimental observations. In contrast, the hydrogenation of the C=C fragment bounded to the protruding surface Co atoms lead to physisorbed butene, weakly coadsorbed on the surface. Here, the spontaneous desorption is predicted for $T \approx 420$ K, i.e only 37 K above the experimental temperature. On $\text{Al}_{13}\text{Fe}_4(010)$, the hydrogenation of the C=C fragment bounded to the protruding surface Fe atom does not lead to physisorbed butene, but to di- σ -butene (Tab. 4), rather strongly coadsorbed at the surface.

To summarize, the comparison of the alkene adsorption energies on $\text{Al}_{13}\text{Co}_4(100)$ and $\text{Al}_{13}\text{Fe}_4(010)$ show a clear difference between the Fe and Co centers, the stronger adsorption of butadiene on $\text{Al}_{13}\text{Fe}_4(010)$ than on $\text{Al}_{13}\text{Co}_4(100)$ being consistent with the higher activity of the $\text{Al}_{13}\text{Fe}_4$ catalyst²¹. For both $\text{Al}_{13}\text{Co}_4(100)$ and $\text{Al}_{13}\text{Fe}_4(010)$ pseudo 10-fold surfaces, the hydrogenation reaction is calculated to be thermodynamically possible. However, the reaction path is expected to be different between the two compounds. This assumption relies on the different adsorption properties of these two surfaces, especially for atomic hydrogen – the B4 site, which has been identified as critical in the case of the semi-hydrogenation of acetylene on $\text{Al}_{13}\text{Co}_4(100)$ ³³ is not favorable on $\text{Al}_{13}\text{Fe}_4(010)$ – and on the dissimilar butene adsorption modes on the two compounds, as well

as the different butene distributions measured experimentally²¹.

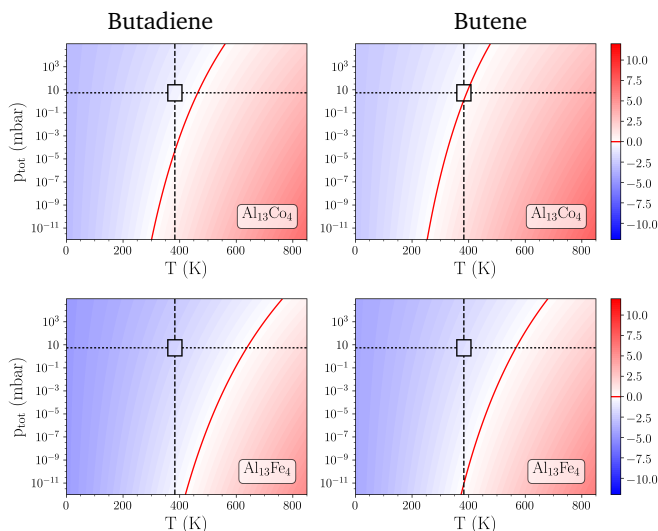


Fig. 4 Adsorption free enthalpies (in eV) for butadiene and butene on the pseudo 10-fold surface of the hydrogenated $\text{Al}_{13}\text{TM}_4$ catalysts, within the PBE approach. Surfaces are covered with butadiene and hydrogen (1 C_4H_6 molecule + 6 H atoms per surface cell). The reaction conditions of Ref. ²¹ (5 mbar, 383 K) are dotted, dashed and squared.

4 Conclusions

In this study, we rationalized the catalytic behavior of the $\text{Al}_{13}\text{Co}_4(100)$ and $\text{Al}_{13}\text{Fe}_4(010)$ surfaces towards butadiene partial hydrogenation. On the basis of surface phase diagrams determined through DFT calculations, we demonstrate that the (P, T, μ_{Al}) conditions where the $\text{Al}_{13}\text{Co}_4(100)$ dense Al-rich flat termination is the most stable narrows as the pressure increases and the temperature decreases. Moreover, based on catalytic experiments, the dense Al-rich flat termination of $\text{Al}_{13}\text{Co}_4(100)$ is unlikely under hydrogenation conditions, the adsorption of C_4H_6 inhibiting any further adsorption of hydrogen at the surface, which prevents butadiene hydrogenation. According to atomistic thermodynamics, the reaction conditions promote a nanostructured surface termination, in the form of highly cohesive clusters emerging from the bulk lattice.

The comparison of butadiene and butene adsorption energies under thermodynamic conditions relevant to the reaction on $\text{Al}_{13}\text{Co}_4(100)$ and $\text{Al}_{13}\text{Fe}_4(010)$, using the same corrugated surface model, reveals different adsorption and coadsorption properties between the two compounds, thus suggesting different catalytic behaviors. On $\text{Al}_{13}\text{Co}_4(100)$ and within the PBE approximation, butene is weakly adsorbed (making it prone to quickly desorb once formed), while it is strongly adsorbed on $\text{Al}_{13}\text{Fe}_4(010)$. The consideration of the DFT-D3 approximation leads to qualitatively different results: butene may not desorb when chemisorbed through a π bonding involving the Co atoms protruding at the surface. A better agreement with the experimental observation is obtained with the hydrogenation of the C=C fragment adsorbed on the protruding Co atom. Our calculations thus suggest the attack of the π -bonded C=C fragment on the protruding Co atom

first. Reaction conditions are also expected to influence the kinetics, for which further investigation is required. Experimental verification of the predicted nanostructuring requires in situ characterization (e.g. surface X-ray diffraction) to identify the actual working surface under gas pressure conditions.

Acknowledgement

This work is supported by the European Integrated Center for the Development of New Metallic Alloys and Compounds. C.C. acknowledges Synchrotron SOLEIL and Région Grand Est for financial support. E.G. acknowledge financial support through the COMETE project (CONception in silico de Matériaux pour l'Environnement et l'Énergie) co-funded by the European Union under the program FEDER-FSE Lorraine et Massif des Vosges 2014-2020. This work was granted access to the HPC resources of TGCC, CINES and IDRIS under the allocation 99642 attributed by GENCI (Grand Equipement National de Calcul Intensif). High Performance Computing resources were also partially provided by the EXPLOR centre hosted by the University de Lorraine (project 2017M4XXX0108). D.L. thanks IDRIS in Paris, CINES in Montpellier, TGCC in Grenoble (project 609, GENCI/CT8) and PSMN in Lyon for CPU time and assistance. He thanks also the CPER/SYSPROD 2015-2022 project (N°2019-AURA-P5B) and AXELERA Pôle de Compétitivité for financial support (PSMN Data Center).

Notes and references

- 1 F. Studt, F. Abild-Pedersen, T. Bligaard, R. Z. Sorensen, C. H. Christensen and J. K. Norskov, *Science*, 2008, **320**, 1320–1322.
- 2 M. Armbrüster, K. Kovnir, M. Friedrich, D. Teschner, G. Wowsnick, M. Hahne, P. Gille, L. Szentmiklosi, M. Feuerbacher, M. Heggen, F. Girgsdies, D. Rosenthal, R. Schlögl and Y. Grin, *Nat. Mater.*, 2012, **11**, 690–693.
- 3 F. Studt, I. Sharafutdinov, F. Abild-Pedersen, C. Elkjaer, J. Hummelshoj, S. Dahl, I. Chorkendorff and J. Norskov, *Nat. Chem.*, 2014, **6**, 320–324.
- 4 L. Piccolo and L. Kibis, *J. Catal.*, 2015, **332**, 112.
- 5 D. Torelli, S. Francis, J. Crompton, A. Javier, J. Thompson, B. Brunshwig, M. Soriaga and N. Lewis, *ACS Catal.*, 2016, **6**, 2100–2104.
- 6 S. Furukawa and T. Komatsu, *ACS Catal.*, 2017, **7**, 735–765.
- 7 A. Dasgupta and R. M. Rioux, *Catal. Today*, 2019, **330**, 2–15.
- 8 M. Friedrich, S. Alarcon-Villaseca, L. Szentmiklosi, D. Teschner and M. Armbrüster, *Materials*, 2013, **6**, 2958–2977.
- 9 L. Zou, J. Fan, Y. Zhou, C. Wang, J. Li, Z. Zou and H. Yang, *Nano Research*, 2015, **8**, 2777–2788.
- 10 E. Antolini, *Appl. Catal. B*, 2017, **217**, 201–213.
- 11 J. Hafner and M. Krajci, *Acc. Chem. Res.*, 2014, **47**, 3378–3384.
- 12 T. Yamada, T. Kojima, E. Abe, S. Kameoka, Y. Murakami, P. Gille and A. P. Tsai, *J. Am. Chem. Soc.*, 2018, **140**, 3838–3841.
- 13 N. F. Mott and H. Jones, *The theory of the properties of metals*

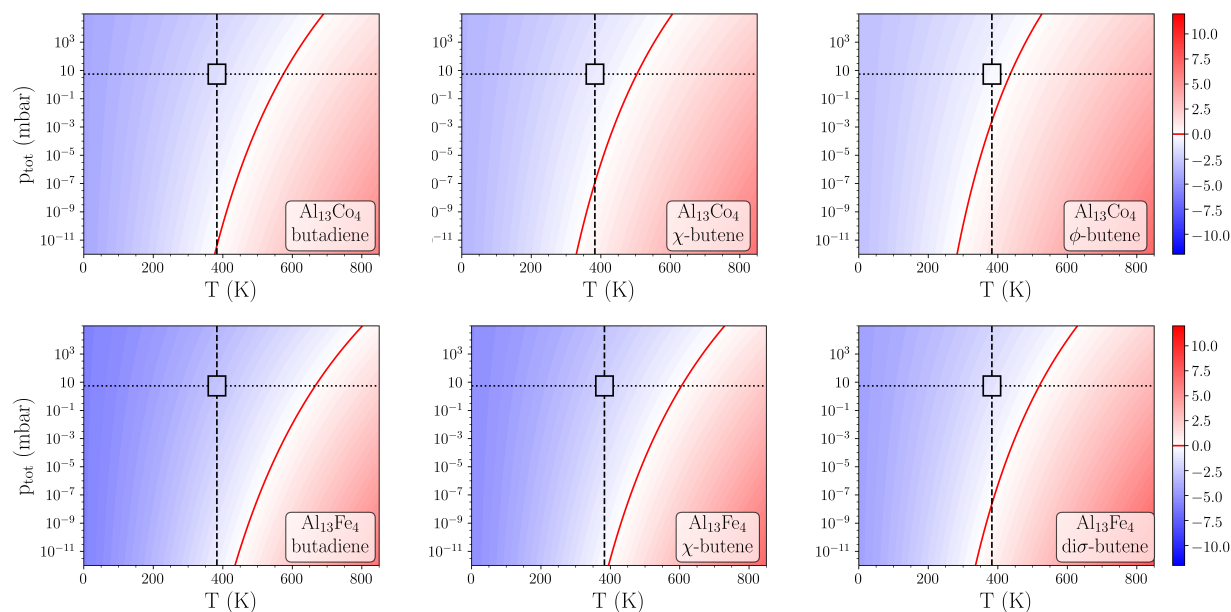
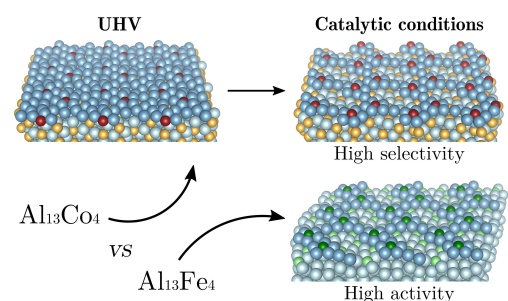


Fig. 5 Adsorption free enthalpies (in eV) for butadiene and butene on the pseudo 10-fold surface of the hydrogenated $\text{Al}_{13}\text{TM}_4$ catalysts, within the DFT-D3 approach. Surfaces are covered with butadiene and hydrogen (1 C_4H_6 molecule + n H atoms per surface cell, $n = 6$ for $\text{Al}_{13}\text{Co}_4(100)$ and $n = 8$ for $\text{Al}_{13}\text{Fe}_4(010)$). The reaction conditions of Ref. ²¹ (5 mbar, 383 K) are squared. χ = chemisorbed; ϕ = physisorbed.

- and alloys, Oxford: The Clarendon press, 1936.
- 14 R. Nesper, *Z. Anorg. Allg. Chem.*, 2014, **640**, 2639–2648.
 - 15 J. Osswald, R. Giedigkeit, R. E. Jentoft, M. Armbrüster, F. Girgsdies, K. Kovnir, T. Ressler, Y. Grin and R. Schlögl, *J. Catal.*, 2008, **258**, 210.
 - 16 K. Kovnir, M. Armbrüster, D. Teschner, T. Venkov, L. Szentmiklósi, F. Jentoft, A. Knop-Gericke, Y. Grin and R. Schloegl, *Surf. Sci.*, 2009, **603**, 1784–1792.
 - 17 G. Somorjai and M. V. Hove, *Prog. Surf. Sci.*, 1989, **30**, 201–231.
 - 18 T. G. Akhmetshina, V. A. Blatov, D. M. Proserpio and A. P. Shevchenko, *Acc. Chem. Res.*, 2018, **51**, 21–30.
 - 19 M. Armbrüster, K. Kovnir, Y. Grin, R. Schlögl, P. Gille, M. Heggen and M. Feuerbacher, 2009.
 - 20 L. Piccolo, *Chem. Commun.*, 2013, **49**, 9149–9151.
 - 21 L. Piccolo, C. Chatelier, M.-C. de Weerd, F. Morfin, J. Ledieu, V. Fournée, P. Gille and E. Gaudry, *Sci. Tech. Adv. Mater.*, 2019, **20**, 557–567.
 - 22 P. Scheid, C. Chatelier, J. Ledieu, V. Fournée and E. Gaudry, *Acta Crystallogr. A*, 2019, **75**, 314–324.
 - 23 E. Gaudry, C. Chatelier, G. McGuirk, L. S. Loli, M.-C. De-Weerd, J. Ledieu, V. Fournée, R. Felici, J. Drnec, G. Beutier and M. de Boissieu, *Phys. Rev. B*, 2016, **94**, 165406.
 - 24 J. Ledieu, E. Gaudry, M.-C. de Weerd, R. D. Diehl and V. Fournée, *Mater. Res. Soc. Symp. Proc.*, 2012, **1517**.
 - 25 H. Shin, K. Pussi, É. Gaudry, J. Ledieu, V. Fournée, S. Alarcón-Villaseca, J.-M. Dubois, Y. Grin, P. Gille, W. Moritz and R. Diehl, *Phys. Rev. B*, 2011, **84**, 085411 (1to11).
 - 26 J. Ledieu, E. Gaudry, L. N. S. Loli, S. A. Villaseca, M.-C. de Weerd, M. Hahne, P. Gille, Y. Grin, J.-M. Dubois and V. Fournée, *Phys. Rev. Lett.*, 2013, **110**, 076102.
 - 27 J. Grin, U. Burkhardt, M. Ellner and K. Peters, *J. Alloys Compd.*, 1994, **206**, 243–247.
 - 28 J. Grin, U. Burkhardt, M. Ellner and K. Peters, *Z. Kristallogr.*, 1994, **209**, 479–487.
 - 29 Y. Grin, B. Bauer, U. Burkhardt, R. C. Gil, J. Dolinsek, M. Feuerbacher, P. Gille, F. Haarmann, M. Heggen, P. Jeglic, M. Mueller, S. Paschen, W. Schnelle and S. Vrtnik, *o-Co₄Al₁₃, a Low-Scale Prototype of Complex Metallic Alloy*, European Congress on Advanced Materials and Processes, Nürnberg, Germany, 2007.
 - 30 U. Burkhardt, M. Ellner and J. Grin, *Powder Diffr.*, 1996, **11**, 123.
 - 31 P. Jeglic, S. Vrtnik, M. Bobnar, M. Klanjek, B. Bauer, P. Gille, Y. Grin, F. Haarmann and J. Dolinsek, *Phys. Rev. B*, 2010, **82**, 104201.
 - 32 P. Jeglic, M. Heggen, M. Feuerbacher, B. Bauer, P. Gille and F. Haarmann, *J. Alloys Compd.*, 2009, **480**, 141–143.
 - 33 M. Krajčí and J. Hafner, *J. Catal.*, 2011, **278**, 200–207.
 - 34 D. Kandaskalov, V. Fournée, J. Ledieu and E. Gaudry, *J. Phys. Chem. C*, 2017, **121**, 18738–18745.
 - 35 P. Priputen, M. Kusý, M. Drienovský, D. Janičkovič, R. Čička, I. Černíčková and J. Janovec, *J. Alloys Compd.*, 2015, **647**, 486–497.
 - 36 M. Mihalkovič and M. Widom, *Phys. Rev. B*, 2007, **75**, 014207.
 - 37 C. L. Henley, *J. Non-Cryst. Solids*, 1993, **153-154**, 172.
 - 38 *Complex Metallic Alloys: Fundamentals and Applications*, ed. J.-M. Dubois and E. Belin-Ferré, Wiley-VCH, Weinheim, 2011.
 - 39 H. Chen, L. Luo, J. Qiang, Y. Wang and C. Dong, *Philos. Mag.*, 2014, **94**, 1463–1477.
 - 40 K. Miyazaki, V. Yannello and D. Fredrickson, *Z. Kristallogr. - Crystalline Materials*, 2017, **232**, 487–496.

- 41 V. Blum, L. hammer, C. Schmidt, O. Wieckhorst, S. Müller and K. Heinz, *Phys. Rev. Lett.*, 2002, **89**, 266102.
- 42 J. Kitchin, K. Reuter and M. Scheffler, *Phys. Rev. B*, 2008, **77**, 075437.
- 43 P. E. Blochl, *Phys. Rev. B*, 1994, **50**, 17953–17979.
- 44 J. P. Perdew, K. Burke and M. Ernzerhof, *Phys. Rev. Lett.*, 1996, **77**, 3865.
- 45 A. Patra, J. E. Bates, J. Sun and J. P. Perdew, *PNAS*, 2017, **114**, E91.
- 46 S. Grimme, S. Ehrlich and L. Goerigk, *J. Comput. Chem.*, 2011, **32**, 1456.
- 47 H. J. Monkhorst and J. D. Pack, *Phys. Rev. B*, 1976, **13**, 5188–5192.
- 48 K. reuter and M. Scheffler, *Phys. Rev. B*, 2001, **65**, 035406.
- 49 F. Bechstedt, *Principles of surface physics*, Springer, Berlin, 2003.
- 50 K. Reuter, C. Stampfl, M. Ganduglia-Pirovano and M. Scheffler, *Chem. Phys. Letters*, 2002, **352**, 311.
- 51 K. Reuter and M. Scheffler, *Phys. Rev. B*, 2003, **68**, 045407.
- 52 S. Posada-Pérez, F. Vinesa, R. Valeroa, J. A. Rodriguez and F. Illas, *Surf. Sci.*, 2017, **656**, 24–32.
- 53 S. Gauthier and P. Sautet, *J. Phys. Chem. C*, 2017, **118**, 4181–4188.
- 54 E.-T. Henig, H. Lukas and G. Petzow, *Z Metallkd*, 1980, **71**, 398e402.
- 55 B. Sundman, I. Ohnuma, N. Dupin and U. K. S. Fries, *Acta Mater.*, 2009, **57**, 2896.
- 56 D. Kandaskalov, V. Fournée, J. Ledieu and E. Gaudry, *J. Phys. Chem. C*, 2014, **118**, 23032–2304.
- 57 B. Hammer and J. K. Norskov, *Surf. Sci.*, 1995, **343**, 211.
- 58 M. Andersen, S. Levchenko, M. Scheffler and K. Reuter, *ACS Catal.*, 2019, **9**, 2752–2759.
- 59 M. Krajčí and J. Hafner, *J. Catal.*, 2012, **295**, 70–80.
- 60 M. Krajčí and J. Hafner, *J. Phys. Chem. C*, 2012, **116**, 6307–6319.
- 61 J. Essen, J. Haubrich, C. Becker and K. Wandelt, *Surf. Sci.*, 2007, **601**, 3472–3480.
- 62 C. Becker, J. Haubrich, K. Wandelt, F. Delbecq, D. Loffreda and P. Sautet, *J. Phys. Chem. C*, 2008, **112**, 14693.
- 63 F. Vigne, J. Haubrich, D. Loffreda, P. Sautet and F. F. Delbecq, *J. Catal.*, 2010, **275**, 129–139.
- 64 L. Nykanen and K. Honkala, *J. Phys. Chem. C*, 2011, 9578–9586.
- 65 M. Meier, J. Ledieu, V. Fournée and E. Gaudry, *J. Phys. Chem. C*, 2017, **121**, 4958–4969.
- 66 B. Mattson, W. Foster, J. Greimann, T. Hoette, N. Le, A. Mirich, S. Wankum, A. Cabri, C. Reichenbacher and E. Schwanke, *J. Chem. Educ.*, 2013, **90**, 613–619.
- 67 D. C. A. Ivarsson, I. G. Aviziotis, T. Keilhauer and M. Armbruster, *Rev. Sci. Instrum.*, 2019, **90**, 014101.



On the basis of DFT, we predict nanostructuring and subsequent catalytic activation of $\text{Al}_{13}\text{Co}_4(100)$ compared to $\text{Al}_{13}\text{Fe}_4(010)$ under reaction conditions

Catalytic activation of a non-noble intermetallic surface through nanostructuring under hydrogenation conditions revealed by atomistic thermodynamics

É. Gaudry^{1*} and C. Chatelier^{1,2}, D. Loffreda³, D. Kandaskalov⁴, A. Coati², L. Piccolo⁵

¹ *Université de Lorraine, CNRS, IJL, F-54000 Nancy, France*

² *Synchrotron SOLEIL, LOrme des Merisiers, Saint-Aubin, France*

³ *Univ. Lyon - Ens de Lyon, CNRS Univ. Lyon 1, F-69342 Lyon, France*

⁴ *Aix Marseille Univ, Univ Toulon, CNRS, IM2NP, Marseille, France*

⁵ *Univ Lyon, Université Claude Bernard - Lyon 1, France*

E-mail: Emilie.Gaudry@univ-lorraine.fr

List of Figures

S1	Surface structures considered for the investigation of the surface stability of the P^{corr} model ($\text{Al}_{13}\text{Co}_4(100)$) as a function of the H_2 pressure and temperature. Color code: Al \rightarrow lightblue, Co \rightarrow dark blue.	S7
S2	Surface structures considered for the investigation of the surface stability of the P^{flat} model ($\text{Al}_{13}\text{Co}_4(100)$) as a function of the H_2 pressure and temperature. Color code: Al \rightarrow lightblue, Co \rightarrow dark blue.	S8
S3	Average adsorption energy of hydrogen atoms per surface cell, as a function of the number of hydrogen atoms in the surface cell.	S8
S4	Surface structures considered for the investigation of the surface stability of the P^{corr} model ($\text{Al}_{13}\text{Co}_4(100)$) as a function of the H_2 pressure and temperature. Color code: Al \rightarrow lightblue, Co \rightarrow dark blue.	S9
S5	Surface structures considered for the investigation of the surface stability of the P^{corr} model ($\text{Al}_{13}\text{Co}_4(100)$) as a function of the H_2 pressure and temperature. Color code: Al \rightarrow lightblue, Co \rightarrow dark blue.	S9
S6	Surface structures considered for the investigation of co-adsorption on $\text{Al}_{13}\text{Fe}_4(010)$. Color code: Al \rightarrow lightblue, Fe \rightarrow orange.	S10
S7	Optimal hydrogen coverage on $\text{Al}_{13}\text{Fe}_4(010)$, calculated within the PBE approximation, as a function of the temperature for 3 different pressures: 10^{-10} mbar, 5 mbar and 50 bar.	S10
S8	Optimal hydrogen coverage on $\text{Al}_{13}\text{Fe}_4(010)$, calculated within the DFT-D3 approximation, as a function of the temperature for 3 different pressures: 10^{-10} mbar, 5 mbar and 50 bar.	S11
S9	Surface phase diagrams and optimal hydrogen coverages (number of hydrogen atoms in the surface cell) for $\text{Al}_{13}\text{Co}_4(100)$ under reaction conditions. The red line corresponds to $\gamma_{\text{cover}}^{\text{P}^{\text{corr}}}(P, T, \mu_{\text{Al}}) - \gamma_{\text{cover}}^{\text{P}^{\text{flat}}}(P, T, \mu_{\text{Al}}) = 0$	S12

List of Tables

S1	Cell parameters and cohesive energies for bulk Al, Co, Fe.	S4
S2	Principal moments of inertia ($\text{kg}\cdot\text{m}^2$), taken from Refs. ^{1,2} for butadiene and 1-butene, respectively	S4
S3	Atomic hydrogen adsorption energies (eV) for Al-Al bridge sites calculated on the flat surface model for $\text{Al}_{13}\text{Co}_4(100)$	S7

S1 - Computational details

S1.1 Cohesive energies

Table S1: Cell parameters and cohesive energies for bulk Al, Co, Fe.

		a (Å)	b (Å)	c (Å)	β ($^\circ$)	E (eV)
Al (fcc)	PBE	4.04	-	-	-	-3.52
	D3	4.04	-	-	-	-3.84
	exp.	4.05	-	-	-	-3.39 ^{3,4}
Co (hcp)	PBE	2.49	-	4.02	-	-5.24
	D3	2.47	-	3.98	-	-5.67
	exp.	2.51	-	4.07	-	-4.39 ^{4,5}
Fe (bcc)	PBE	2.76	-	-	-	-4.38
	D3	2.83	-	-	-	-5.25
	exp.	2.93	-	-	-	-4.28 ^{4,6}

S1.2 Partition functions

The quantities $z_{*trans}^{\mathcal{X}}$, $z_{rot}^{H_2}$ and $z_{rot}^{C_4H_x}$ of the \mathcal{X} , H_2 and C_4H_x species in the gas phase are, respectively, $(\frac{2\pi m_{\mathcal{X}} k_B T}{h^2})^{\frac{3}{2}}$, $\frac{T}{\sigma \theta_r}$ and $(\frac{8\pi^2 k_B T}{h^2})^{\frac{3}{2}} \frac{\sqrt{\pi I_a I_b I_c}}{\sigma}$ with $\sigma = 2$, $\theta_r = 87.6$ K,⁷ I_i ($i \in \{a, b, c\}$) the principal moments of inertia, taken from Refs.^{1,2} for butadiene and 1-butene, respectively (Tab. S1).

Table S2: Principal moments of inertia (kg·m²), taken from Refs.^{1,2} for butadiene and 1-butene, respectively

	I_a	I_b	I_c
butadiene	2.01×10^{-46}	1.89×10^{-45}	2.09×10^{-45}
1-butene	5.54×10^{-46}	1.54×10^{-45}	1.99×10^{-45}

S1.3 Surface energy calculations

According to Ref.,⁸ the surface energy γ_{clean} of an elemental metal can be calculated using the following method. We consider a solid with a finite number n of infinitely extended

planar atomic layers, and a slab of finite area A embedded in this solid. The slab has n layers, each with N_ℓ atoms. The surface energy is given by

$$\gamma_{clean} = \lim_{n \rightarrow \infty} \frac{E_{slab(n)} - nN_\ell E_{bulk}}{2A} \quad (1)$$

where $E_{slab}(n)$ is the total energy of the slab and E_{bulk} is the energy per atom of the infinite bulk. The factor of $\frac{1}{2}$ in this equation comes from the fact that the slab is bounded by two symmetric surfaces.

In the case of compounds, the stoichiometry of the slab is in general different from the one of the bulk. The surface energy is then determined as a function of the chemical potentials.⁹ The chemical potential of species i (μ_i) is defined as the derivative of the Gibbs free enthalpy G for a given phase with respect to the number of particles i and fixed numbers of other particles $\{N_j\}$ apart from N_i :

$$\mu_i = \left(\frac{\partial G}{\partial N_i} \right)_{P,T,N_j} \quad (2)$$

For condensed states, the Gibbs free enthalpy per particle can be taken as the total energy per atom calculated at $T = 0$ K, i.e. as the cohesive energy (E_{coh} = the energy required to separate the elements into neutral atoms at $T = 0$ K and atmospheric pressure P). Indeed, the Gibbs free enthalpy $G(T, P, N)$ can be expressed using the Helmholtz free energy $F(T, V, N)$: $G(T, P, N) = F(T, V, N) + PV$. Under normal pressure ($\simeq 1$ atm), the difference between the Helmholtz free energy F and the Gibbs free energy G ($F - G = -PV$) is almost zero for a solid. In addition, the temperature-dependent term is assumed to be negligible, based on the argument that there is a partial cancellation of the TS term (S is the entropy) with the contributions of the lattice vibrations to the internal energies ($3k_B T \sum N_i$), at least in the limit of the validity of the equipartition theorem.

In the case of a simple metal, the previous statements imply that the chemical potential is simply given by the cohesive energy. For example, the chemical potential for Al in bulk Al is $\mu_{Al}^{bulk} = E_{coh}^{Al}$. In the case of a compound, the chemical potential is given by the Gibbs phase

rule (equilibrium conditions). For Al_xCo_y , it implies that : $(x + y)\mu_{\text{Al}_x\text{Co}_y}^{bulk} = x\mu_{\text{Al}} + y\mu_{\text{Co}}$ where μ_{Al} and μ_{Co} are the chemical potentials of Al and Co in Al_xCo_y .

When compound surfaces are modeled by symmetric slabs, the surface energies are given by

$$\gamma_{clean} = \lim_{slab} \frac{E(N_i) - \sum N_i \mu_i}{2A} \quad (3)$$

where μ_i and N_i are the chemical potentials and number of atoms of type i in the slab. In the previous equation, the numerator can be understood as the difference between the total energy of the slab and the energy of the corresponding bulk with the same stoichiometry.

S2 - Adsorption and coadsorption on $\text{Al}_{13}\text{Co}_4(100)$

S2.1 - Hydrogen adsorbed on $\text{Al}_{13}\text{Co}_4(100)$: P^{corr} model

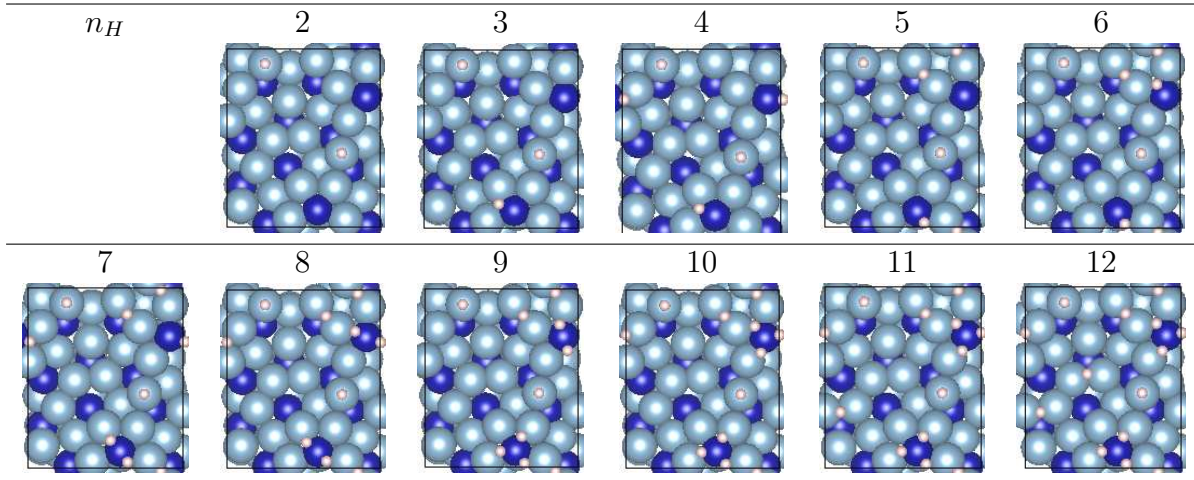


Figure S1: Surface structures considered for the investigation of the surface stability of the P^{corr} model ($\text{Al}_{13}\text{Co}_4(100)$) as a function of the H_2 pressure and temperature. Color code: Al \rightarrow lightblue, Co \rightarrow dark blue.

S2.2 - Hydrogen adsorbed on $\text{Al}_{13}\text{Co}_4(100)$: P^{flat} model

Table S3: Atomic hydrogen adsorption energies (eV) for Al-Al bridge sites calculated on the flat surface model for $\text{Al}_{13}\text{Co}_4(100)$.

Site	PBE	DFT-D3
B'4	-0.11	-0.18
B'1	-0.16	-0.23
B'2	-0.16	-0.22
B'6	-0.01	-0.06
B'3	-0.15	-0.20
B'5	-0.10	-0.16
B'7	0.02	-0.03

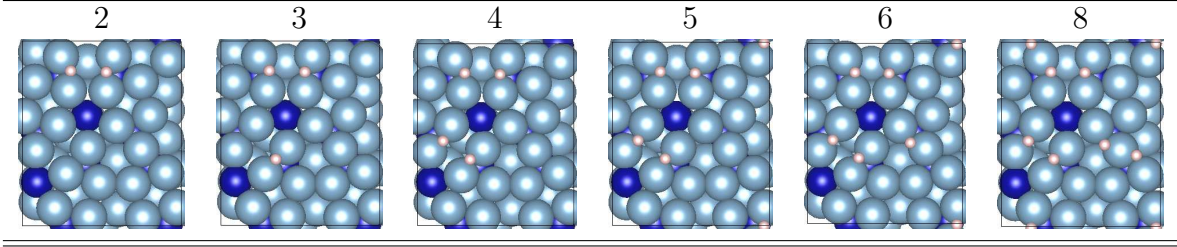


Figure S2: Surface structures considered for the investigation of the surface stability of the P^{flat} model ($\text{Al}_{13}\text{Co}_4(100)$) as a function of the H_2 pressure and temperature. Color code: Al \rightarrow lightblue, Co \rightarrow dark blue.

S2.3 - Average hydrogen adsorption energies

The progressive filling of less stable adsorption sites leads to a gradual decrease of the average adsorption energies per hydrogen atom (Fig. S3). In the case of the P^{flat} model, the adsorption energies on the well separated sites B'1, B'2 and B'4 are very similar, leading to a small decrease in the adsorption energy as a function of hydrogen coverage. The decrease is much more pronounced in the case of the nanostructured surface (P^{corr} model). In this case, we only considered adsorption on the pentagonal bi-pyramid clusters emerging at the surface (sites T_i with $i \in \{1, 2, 3\}$ and B_j , with $j \in \{1, 2, 3\}$ for $\text{Al}_{13}\text{Fe}_4$, and $j \in \{1, 2\}$ for $\text{Al}_{13}\text{Co}_4$).

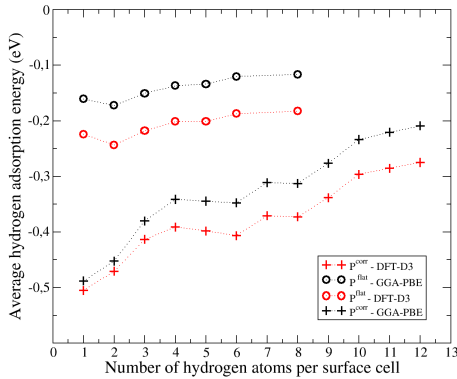


Figure S3: Average adsorption energy of hydrogen atoms per surface cell, as a function of the number of hydrogen atoms in the surface cell.

S2.4 - Co-adsorption on $\text{Al}_{13}\text{Co}_4(100)$: P^{corr} model

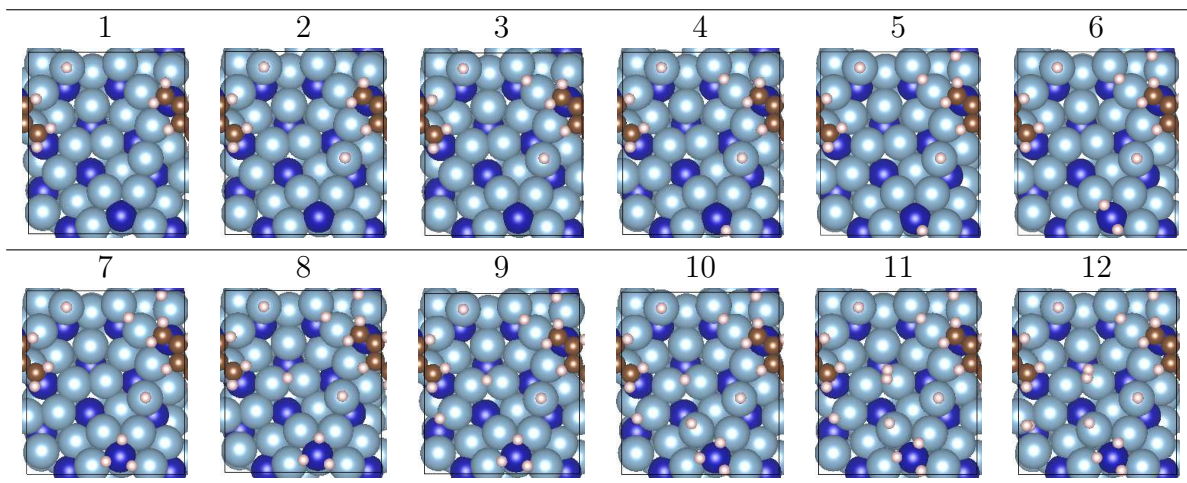


Figure S4: Surface structures considered for the investigation of the surface stability of the P^{corr} model ($\text{Al}_{13}\text{Co}_4(100)$) as a function of the H_2 pressure and temperature. Color code: Al → lightblue, Co → dark blue.

S2.5 - Co-adsorption on $\text{Al}_{13}\text{Co}_4(100)$: P^{flat} model

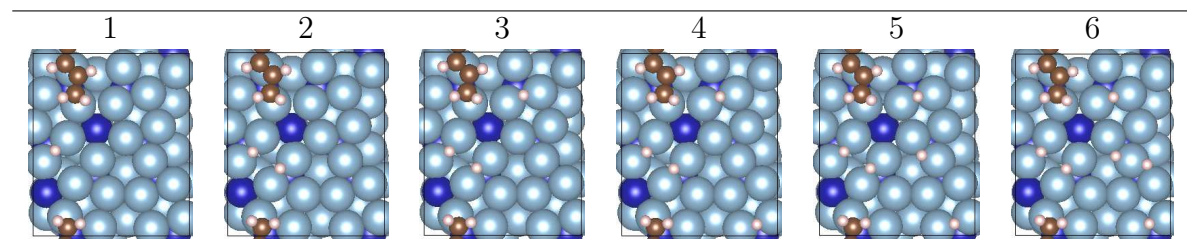


Figure S5: Surface structures considered for the investigation of the surface stability of the P^{corr} model ($\text{Al}_{13}\text{Co}_4(100)$) as a function of the H_2 pressure and temperature. Color code: Al → lightblue, Co → dark blue.

S3 - Coadsorption on $\text{Al}_{13}\text{Fe}_4(010)$

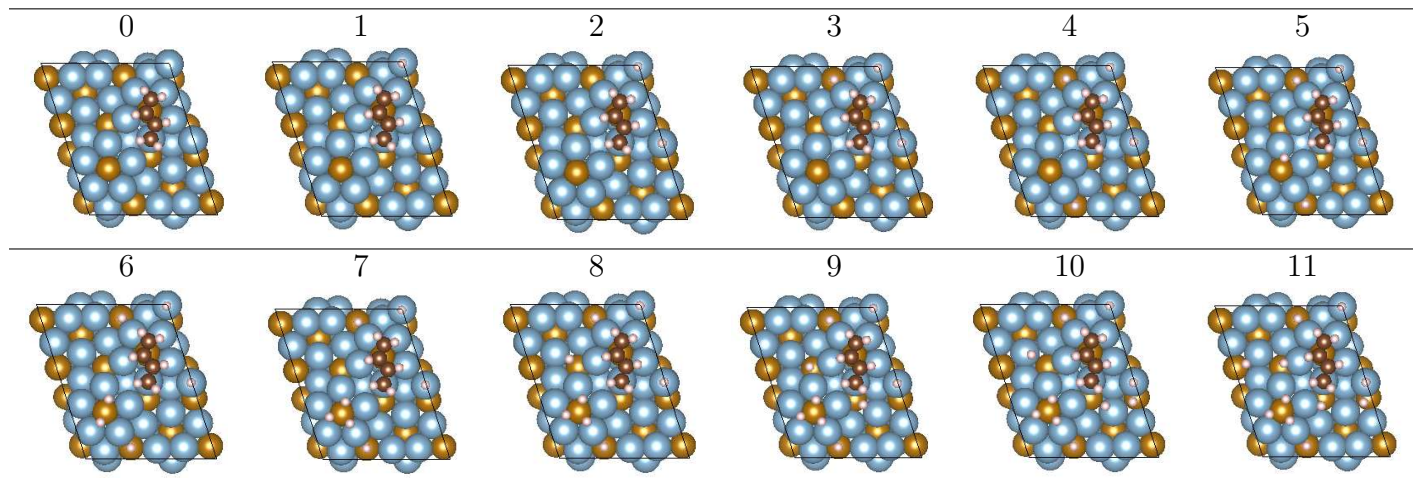


Figure S6: Surface structures considered for the investigation of co-adsorption on $\text{Al}_{13}\text{Fe}_4(010)$. Color code: Al \rightarrow lightblue, Fe \rightarrow orange.

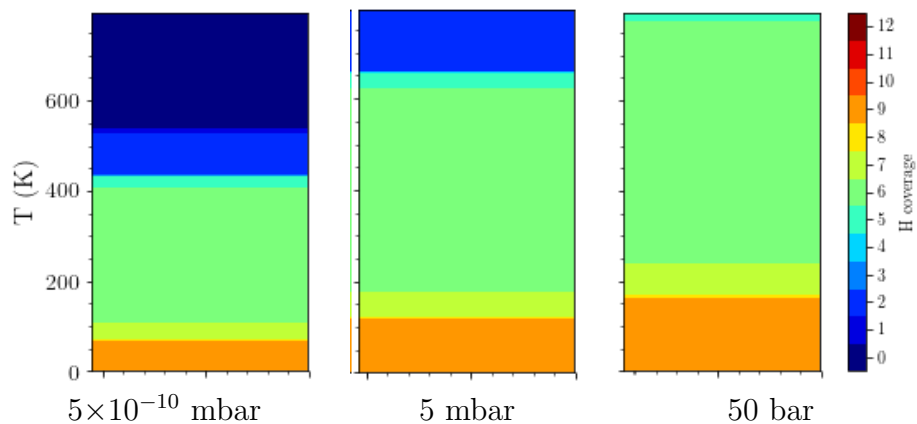


Figure S7: Optimal hydrogen coverage on $\text{Al}_{13}\text{Fe}_4(010)$, calculated within the PBE approximation, as a function of the temperature for 3 different pressures: 10^{-10} mbar, 5 mbar and 50 bar.

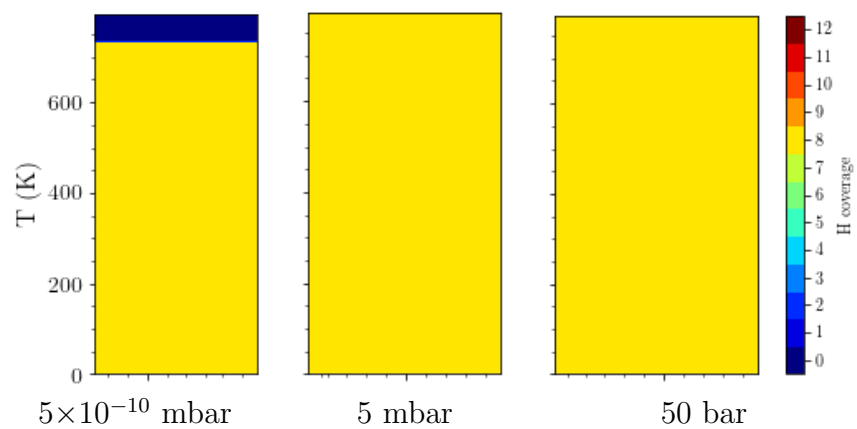


Figure S8: Optimal hydrogen coverage on $\text{Al}_{13}\text{Fe}_4(010)$, calculated within the DFT-D3 approximation, as a function of the temperature for 3 different pressures: 10^{-10} mbar, 5 mbar and 50 bar.

S4 Surface phase diagrams

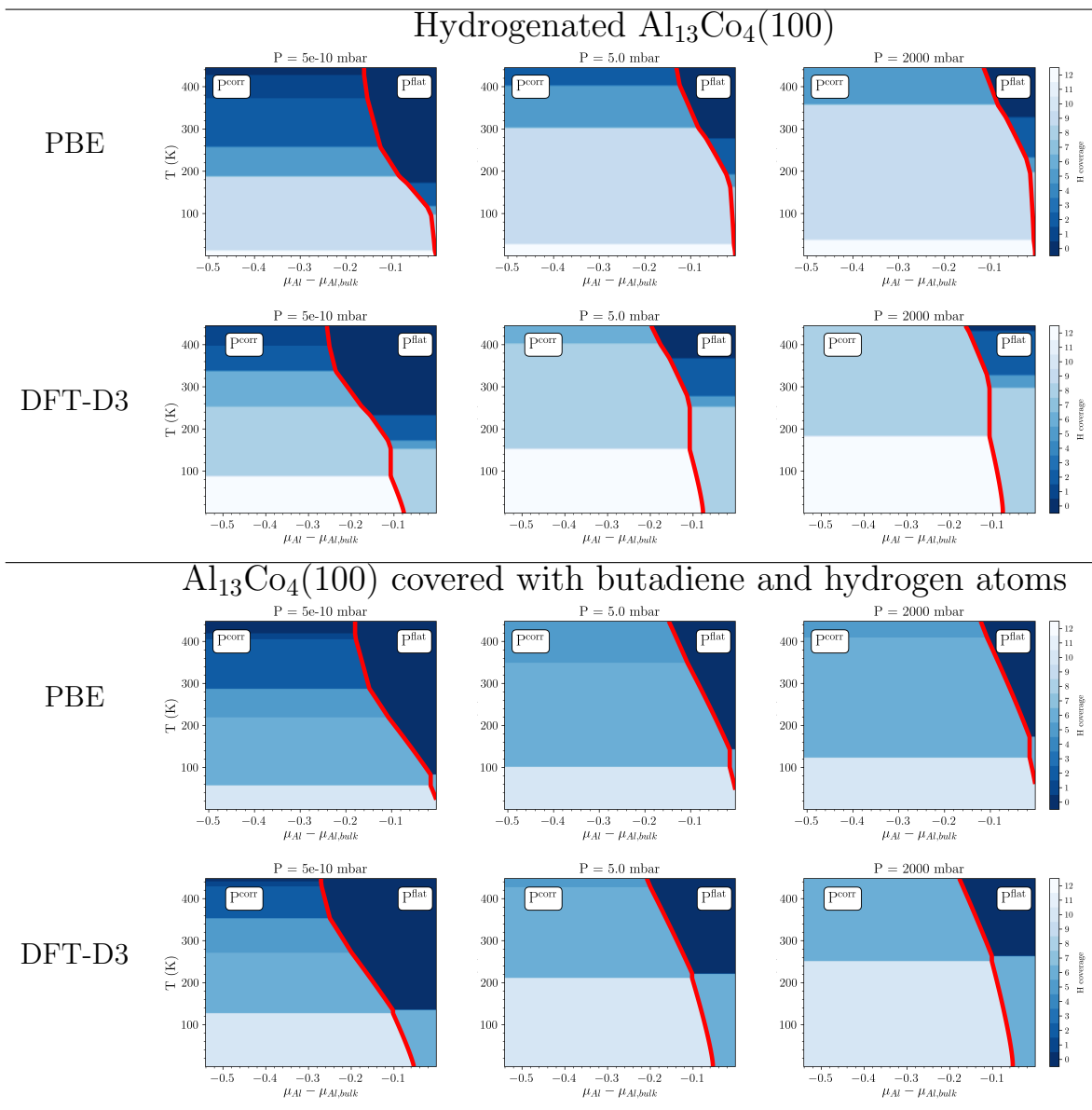


Figure S9: Surface phase diagrams and optimal hydrogen coverages (number of hydrogen atoms in the surface cell) for $\text{Al}_{13}\text{Co}_4(100)$ under reaction conditions. The red line corresponds to $\gamma_{cover}^{P^{corr}}(P, T, \mu_{Al}) - \gamma_{cover}^{P^{flat}}(P, T, \mu_{Al}) = 0$.

S5 Bader charge calculations

Bader charge calculations reveal that butadiene adsorption comes along with a charge depletion on the TM and Al atoms involved in the π bonding, driven by the electronegativity difference between the adsorbate and the metal : -0.75 e and -0.32 e on Co and Al, respectively, for $\text{Al}_{13}\text{Co}_4(100)$, -0.63 e and -0.38 e on Fe and Al, respectively, for $\text{Al}_{13}\text{Fe}_4(010)$. This corresponds to a charge accumulation on the corresponding butadiene carbon atoms : 0.21 e and 0.29 e on carbon atoms π -bonded to the Co and Al atoms, respectively, for $\text{Al}_{13}\text{Co}_4(100)$, while it is 0.22 e and 0.39 e on carbon atoms π -bonded to the Fe and Al atoms, respectively, for $\text{Al}_{13}\text{Fe}_4(010)$.

References

- (1) Craig, N. C.; Groner, P.; McKean, D. C. Equilibrium Structures for Butadiene and Ethylene: Compelling Evidence for Pi-Electron Delocalization in Butadiene. *J. Phys. Chem. A* **2006**, *110*, 7461–7469.
- (2) Bouchy, A.; Roussy, G.; Ledoux, M.; Gault, F. Interpretation of the rotational spectra of multideuteriated species of but-1-ene for the study of catalytic mechanisms by microwave spectroscopy. *J. de Chim. Physique* **1979**, *76*, 357–363.
- (3) Cooper, A. S. Precise Lattice Constants of Germanium, Aluminum, Gallium Arsenide, Uranium, Sulphur, Quartz and Sapphire. *Acta Crystallogr.* **1962**, *15*, 578–582.
- (4) Kittel, C. *Introduction to Solid State Physics*, 7th ed.; John Wiley & Sons: USA, 1996.
- (5) Hull, A.; Davey, W. Crystal structure of cobalt. *Physical Review* **1919**, *14*, 54.
- (6) Basinski, Z.; Hume-Rothery, W.; Sutton, A. The lattice expansion of iron. *Proceedings of the Royal Society of London, Series A: Mathematical and Physical Sciences* **1955**, *229*, 459–467.

- (7) Atkins, P.; Paula, J. *Physical Chemistry, 9th edition*; Oxford University press: Oxford, 2010.
- (8) Patra, A.; Bates, J. E.; Sun, J.; Perdew, J. P. Properties of real metallic surfaces: Effects of density functional semilocality and van der Waals nonlocality. *PNAS* **2017**, *114*, E91.
- (9) Bechstedt, F. *Principles of surface physics*; Springer: Berlin, 2003.